Inorganic Chemistry

pubs.acs.org/IC

Featured Article

P_2S_5 Reactive Flux Method for the Rapid Synthesis of Mono- and Bimetallic 2D Thiophosphates $M_{2-x}M'_xP_2S_6$

Daniel G. Chica, Abishek K. Iyer, Matthew Cheng, Kevin M. Ryan, Patrick Krantz, Craig Laing, Roberto dos Reis, Venkat Chandrasekhar, Vinayak P. Dravid, and Mercouri G. Kanatzidis*

Cite This: *Inorg. Chem.* 2021, 60, 3502−3513

Read Online

ACCESS | Metrics & More | Article Recommendations | Supporting Information

ABSTRACT: We report a reactive flux technique using the common reagent P_2S_5 and metal precursors developed to circumvent the synthetic bottleneck for producing high-quality single- and mixed-metal two-dimensional (2D) thiophosphate materials. For the monometallic compound, $M_2P_2S_6$ (M = Ni, Fe, and Mn), phase-pure materials were quickly synthesized and annealed at 650 °C for 1 h. Crystals of dimensions of several millimeters were grown for some of the metal thiophosphates using optimized heating profiles. The homogeneity of the bimetallic thiophosphates $MM'P_2S_6$ (M, M′ = Ni, Fe, and Mn) was elucidated using energy-dispersive X-ray spectroscopy and Rietveld refinement. The quality of the selected materials was characterized by transmission electron microscopy and atomic force microscopy measurements. We report two novel bimetallic thiophosphates, $MnCoP_2S_6$ and $FeCoP_2S_6$. The $Ni_2P_2S_6$ and $MnNiP_2S_6$ flux reactions were monitored in situ using variable-temperature powder X-ray diffraction to understand the formation reaction pathways. The phases were directly formed in a single step at approximately 375 °C. The work functions of the semiconducting materials were determined and ranged from 5.28 to 5.72 eV.

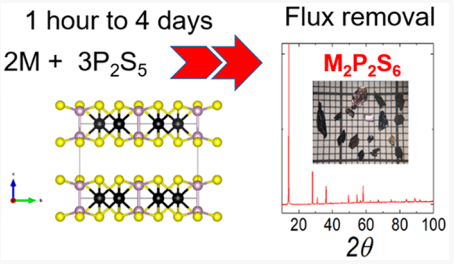

INTRODUCTION

Transition-metal thiophosphates or $M_2P_2Q_6$ (or MPQ_3, where Q = S, Se) are two-dimensional (2D) semiconductors held together by weak van der Waals (vdW) interactions. This broad family of materials can accommodate a wide variety of metals in their structure.[1,2] Because of this flexibility, the physical properties, such as the band gap within the semiconductor region, and magnetic properties can be tuned. Studies of these compounds in the 1980s and 1990s were focused on the intercalation chemistry[3] for Li-ion cathode materials. Since then, scientists have revisited this family and uncovered exotic 2D magnetism,[4−6] 2D ferroelectricity,[7] high-pressure science,[8−10] potential for H_2 storage,[11] and catalysis.[12,13] This ability to tune the magnetic and optical properties has made $M_2P_2Q_6$ attractive for new kinds of studies in line with those of other known 2D materials, such as transition-metal chalcogenides[14] (narrow substitution range) or graphene (low-band-gap materials).[15] These compounds form characteristic slabs with the CdI_2 structure type, which are stacked along one direction and interact only via vdW forces. The slabs comprise ethane-like $[P_2Q_6]^{4-}$ ligands, which are counterbalanced with two octahedrally coordinated metal ions per ligand with an average formal charge of 2+. The structure can accommodate 1+, 2+, 3+, and 4+ metals as well as the $[P_2]^{8+}$ dumbbells that lie at the center of the ethane-like $[P_2Q_6]^{4-}$ ligand. Additionally, the steric flexibility of the $[P_2Q_6]^{4-}$ ligand gives rise to a large composition space, accommodating metal ions as small as Li^{+}[16] and up to as large as Bi^{3+}.[17] Further structural complexity can be introduced in compounds that have the same cation ordering in a single plane but with different stacking sequences. Bimetallic chalcophosphate systems typically feature either ordered M^{+} and M^{3+} cations or two different divalent cations with mixed occupation on the same crystallographic site. The ordered phases include $MM'P_2Se_6$ (M = Cu, Ag, and Li; M′ = Al, Cr, Ga, In, Sb, and Bi)[17−19] and $MM'P_2S_6$ (M = Ag, Cu, Li, and Na; M′ = Cr, In, and Al).[7,20−22] The disordered, alloyed, layered phases that have been studied are typically comprised of alloys containing third-row d-block metals.[23−29] The structures of the compounds in this study are shown in Figure 1.

As suggested in a review by Maksymovych et al., over a thousand publications exist on these compounds. In the review, the authors discuss the various synthetic methods used to obtain these materials. Table 1 summarizes the temperature and duration reported for the synthesis of $M_2P_2S_6$ and $MM'P_2S_6$. As can be inferred from the table, the lowest synthesis steps in making these compounds take from 2 weeks to 3 months to produce phase-pure samples. Often, a problem

Received: December 7, 2020
Published: February 26, 2021

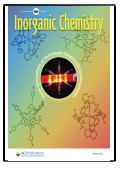

https://dx.doi.org/10.1021/acs.inorgchem.0c03577
Inorg. Chem. 2021, 60, 3502−3513

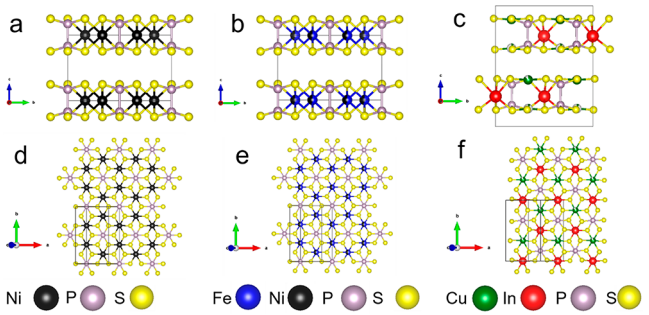

Figure 1. Crystal structures of (a) monometallic ($Ni_2P_2S_6$)[3] and bimetallic (b) disordered ($FeNiP_2S_6$)[27] and (c) ordered ($CuInP_2S_6$)[49] thiophosphate phases viewed down the *a* axis and (d–f) viewed down the axis perpendicular to the basal plane.

arises from the formation of substantial amounts of impurity phases, such as the pyrite form of $Co(P,S)_2$ in $Co_2P_2S_6$ or FeS_2 in $Fe_2P_2S_6$.[30] Relatively high annealing temperatures lead to decomposition of these phases, as observed by Madian et al., who found that heating $Fe_2P_2S_6$ at 900 °C resulted in a mixture of $Fe_2P_2S_6$, Fe_7S_8, and FeS_2. The paper also reported that better crystallinity was obtained by heating the sample slowly (1 °C/min).[31] Large-scale syntheses (>50 g) of $Mn_2P_2S_6$, $Ni_2P_2S_6$, and $Cd_2P_2S_6$ have been successfully performed.[30] Contrarily, >20 g of $Zn_2P_2S_6$ has been successfully achieved, although small amounts of $Zn_4(P_2S_6)_3$ were found as impurities.[30] Homogeneous bimetallics, $MM'P_2S_6$, have been harder to obtain because of the varying degrees of mixed occupation of the two metals that the quasi-ternary phase can tolerate. As shown in Table 1, the reactions should be performed for at least 1 month, and regrinding and reheating are required to obtain pure bimetallic phases. Additionally, the relatively low boiling point temperatures of P and S create a high vapor pressure, which can be dangerous for bulk synthesis. One method of obtaining large single crystals is by chemical vapor transport, where small amounts of iodine (10–30 mg) or chlorine are used as transporting agents, along with stoichiometric amounts of the elements.[2,32] There are reports where crystals of $Ni_2P_2S_6$ are grown in a two-zone horizontal furnace.[4] This method produces large-sized crystals (>1 mm) that are hand-picked for specific measurements. While this method produces high-quality crystals, neutron diffraction studies on $Ni_2P_2S_6$ and $Co_2P_2S_6$ have shown that large streaks are observed in the reciprocal lattice, making it difficult to obtain a good magnetic structure.[4,33] Moreover, these reactions take up to 20 days with controlled heating in a two-zone tube furnace. Therefore, improved synthetic methods to expedite the time to produce pure materials are highly desired.

The flux method has been employed for the synthesis and crystal growth of inorganic solids.[34] The flux dissolves relatively high melting reagents at reduced temperatures, and upon cooling, the product of interest crystallizes out from this molten flux. If the flux is incorporated into the product, it is referred to as a reactive flux. The synthesis of several alkali-metal-containing chalcophosphates has been achieved using the chalcophosphate flux method.[35] This reactive flux has a general composition of $A_2Q/P_2Q_5/Q$ (A = alkali metal; Q = S and Se) and an oxidizing effect on the metal of interest. The simpler form of this flux without the alkali-metal component has been used to synthesize only a few compounds, β-$Bi_4(P_2Se_6)_3$[36] and AMP_2Se_6[19] (A = Cu and Ag; M = Bi and Sb).

Here, we introduce the P_2S_5 flux method for the synthesis and crystal growth of mono- and bimetallic thiophosphates in greatly reduced synthesis times. Several heating profiles were investigated with a fixed metal-to-P_2S_5 ratio to elucidate the crystal growth behavior of the metal thiophosphates from the P_2S_5 flux. Monometallic $M_2P_2S_6$ were synthesized as quickly as 1 h and annealed at 650 °C. The synthesis of bimetallic thiophosphates had varying degrees of success at the two annealing temperatures used. Variable-temperature (VT) powder X-ray diffraction (PXRD) (in situ) measurements on mono- and bimetallic thiophosphates reveals the synthetic pathway for the formation of these compounds.

EXPERIMENTAL SECTION

Chemical Reagents. The following reagents were used as received: manganese powder (99.5%, Alfa Aesar), iron powder (99.9%, Cerac), cobalt powder (99.8%, Cerac), nickel powder (99.9%, Johnson Matthey), copper powder (99.999%, Sigma-Aldrich), zinc powder (99.999%, Sigma-Aldrich), cadmium powder (99.999%, Cerac), indium droplets (99.99%, American elements), magnesium powder (98%, Sigma-Aldrich), phosphorus pentasulfide powder (99%, Sigma-Aldrich), phosphorus chunks (99.999%, Puratronic), and sulfur pieces (99.98%, Aldrich). The solvents used were house deionized (DI) water, anhydrous ethanol (Fisher Chemical), and acetone (99.5%, Fisher Chemical).

Synthesis of Layered Metal Thiophosphates. The layered thiophosphates were synthesized using the reactive P_2S_5 flux method. In a nitrogen-filled glovebox, metal and P_2S_5 powders were loaded into 12.7-mm-outside-diameter and 10.5-mm-inside-diameter fused-

Table 1. Synthetic Conditions of Various Mono- and Bimetallic Thiophosphates from the Literature

compound	temperature profile/duration	method	reference
$Mg_2P_2S_6$	700 °C, 50 h, cooled at 10 °C/h	stoichiometric; Mg, P, S	45
$Mn_2P_2S_6$	600–750 °C, 2 months	stoichiometric; Mn, P, S	3
	650 °C, 120 h, cooled at 1 °C/min		30
$Fe_2P_2S_6$	600–730 °C, 2 months	stoichiometric; Fe, P, S	3
	650 °C, 120 h, cooled at 1 °C/min		30
$Co_2P_2S_6$	400–650 °C, 3 months	stoichiometric; Co, P, S	3
	650 °C, 120 h, cooled at 1 °C/min, additional heating at 750 °C, 168 h		30
$Ni_2P_2S_6$	570–710 °C, 3 months	stoichiometric; Ni, P, S	3
	650 °C, 120 h, cooled at 1 °C/min, additional heating at 750 °C, 168 h, cooled at 1 °C/min		30
$Fe_{0.5}Ni_{0.5}P_2S_6$	700 °C, 1 month, regrinding and reheating required	stoichiometric; Fe, Ni, P, S	27
$Mn_xFe_{2-x}P_2S_6$ ($0 < x < 1$)	700 °C, 2 weeks, followed by slow cooling	stoichiometric; Mn, Fe, P, S	26
$Mn_xNi_{2-x}P_2S_6$ ($0 < x < 1$)	750 °C, 15 days, regrinding and reheating (total time 1 month)	stoichiometric; Mn, Ni, P, S	29
$Co_xNi_{2-x}P_2S_6$ ($0 < x < 1$)	650 °C, no time provided	stoichiometric; Co, Ni, P, S	25

https://dx.doi.org/10.1021/acs.inorgchem.0c03577
Inorg. Chem. 2021, 60, 3502–3513

Table 2. Tabulated Heating Profiles for the Synthesis of Mono- and Bimetallic Thiophosphates Compounds

heating profile abbreviation	heating profile step	metal of the thiophosphate compound made with the heating profile
Heating 1	RT $\xrightarrow{10\text{ h}}$ 650 °C $\xrightarrow{36\text{ h}}$ 650 °C $\xrightarrow{12\text{ h}}$ 250 °C $\xrightarrow{\text{step}}$ RT	Mg, Mn, Fe, Co, Ni, Zn, Cd, CuIn, MnFe, MnCo, MnNi, FeCo, FeNi, CoNi
Heating 2	RT $\xrightarrow{10\text{ h}}$ 650 °C $\xrightarrow{72\text{ h}}$ 650 °C $\xrightarrow{24\text{ h}}$ 250 °C $\xrightarrow{\text{step}}$ RT	Co
Heating 3	650 °C $\xrightarrow{96\text{ h}}$ 650 °C $\xrightarrow{\text{quench}}$ RT	Ni
Heating 4	650 °C $\xrightarrow{1\text{ h}}$ 650 °C $\xrightarrow{96\text{ h}}$ 250 °C $\xrightarrow{\text{step}}$ RT	Ni
Heating 5	RT $\xrightarrow{10\text{ h}}$ 540 °C $\xrightarrow{96\text{ h}}$ 540 °C $\xrightarrow{\text{quench}}$ RT	Co, Ni, MnFe, MnCo, MnNi, FeCo, FeNi, CoNi
Heating 6	RT $\xrightarrow{10\text{ h}}$ 580 °C $\xrightarrow{96\text{ h}}$ 580 °C $\xrightarrow{\text{quench}}$ RT	Co
Heating 7	RT $\xrightarrow{3\text{ h}}$ 350 °C $\xrightarrow{12\text{ h}}$ 350 °C $\xrightarrow{3\text{ h}}$ 650 °C $\xrightarrow{48\text{ h}}$ 650 °C $\xrightarrow{48\text{ h}}$ 350 °C $\xrightarrow{\text{step}}$ RT	CuIn
Heating 8	650 °C $\xrightarrow{1\text{ h}}$ 650 °C $\xrightarrow{\text{quench}}$ RT	Ni, Fe, Mn, Zn

silica tubes with a total charge mass of 2 g. The M (M/M′)-to-P_2S_5 ratio was 2:3 and 1:1:3 for the monometallic and bimetallic thiophosphates, respectively. The amounts used are tabulated in Table S1. The tubes were sealed with an oxy/natural gas torch under a pressure of ~3 × 10^{-3} mbar. After sealing, the tubes were mechanically agitated for 10 min to ensure mixing of the reagents. The tubes were heated using a computer-controlled tube furnace with the heating profiles shown in Table 2. ***Warning!*** *Removal of the flux must be performed in a fume hood because this reaction releases H_2S gas.* In a fume hood, the silica ampule was opened, and the ingot was placed in a 20 mL scintillation vial with 10 mL of a 50:50 (v/v) mixture of DI water and ethanol (50:50 H_2O/EtOH) and heated to ~70 °C for 1 h. If any flux remained, the solution was decanted, 10 mL of 50:50 H_2O/EtOH was added, and the resulting solution was heated for 1 h. After removal of the flux, the product was washed twice with DI water and twice with acetone. The residual thiols were left to off-gas overnight.

$Mg_2P_2S_6$ dissolves in water and 50:50 H_2O/EtOH, so the excess P_2S_5 was removed by subliming the P_2S_5 using a long tube (~25 cm long) and heating the sample at 300 °C for 24 h. No residual P_2S_5 was observed in the sample.

Photoemission Yield Spectroscopy in Air (PYSA). PYSA (AC-2, Riken-Keiki) was used to determine the work function by measuring the valence band maximum energy level. The sample was illuminated by a tunable monochromatic ultraviolet light source (UV, 4.20−6.20 eV) under dry air. Several photoelectrons are generated at each excitation energy by 0.10 eV steps. Photoelectrons are only generated when the photon energy is higher than the work function. The work function value was then determined by determining the onset of the PYSA spectra. The spectra were collected on materials made using **Heating 1** except for $Co_2P_2S_6$ and $CuInP_2S_6$, which were made from **Heating 6** and 7, respectively.

Transmission Electron Microscopy (TEM) Imaging, Selected-Area Electron Diffraction (SAED), and Scanning Transmission Electron Microscopy−Energy-Dispersive X-ray Spectroscopy (STEM−EDS). High-resolution TEM (HRTEM) and SAED were obtained using a JEOL ARM300 microscope at 300 kV along the [001]-zone axis to ascertain the crystalline nature of the $Ni_2P_2S_6$, $Mn_2P_2S_6$, and $MnNiP_2S_6$ systems. STEM−EDS was conducted with an Oxford silicon drift detector to determine the stoichiometry of each respective thiophosphate system. The convergence angle of the STEM probe is 24 mrad, which at 300 keV corresponds to a probe size of 1.1 Å full width at half-maximum (fwhm), and the solid angle of the Oxford detector is 0.98 sr. TEM samples were prepared using mechanical exfoliation. SAED patterns were simulated using *SingleCrystal*. The thiophosphate material for these measurements was made using **Heating 1**.

Device Fabrication and Measurements. Metal thiophosphate crystals were cleaved by mechanical exfoliation using commercial PVC tape (Nitto SPV-224PR-MJ) or a poly(dimethylsiloxane) film (PDMS Gel-film PF-X4 from Gel-Pack). Following cleavage, the flakes adhered to 330 nm SiO_x-coated p-type Si wafers for optical identification by bright-field/dark-field-reflected light microscopy. The residual adhesive was removed by washing the substrate with acetone, methanol, and isopropyl alcohol. Noncontact atomic force microscopy (NC-AFM) was performed using a Park XR-150 microsope with BudgetSensors Tap300Al-G cantilevers. Electrical contacts were made by wetting the top and bottom of the crystal using graphite paint (Ted Pella-PELCO isopropane-based graphite paint) and copper wire. The materials used for these exfoliations and measurements were from **Heating 1**, except for $CuInP_2S_6$, which was from **Heating 7**.

RESULTS AND DISCUSSION

P_2S_5 Flux and Stability of Thiophosphate Compounds. The excess P_2S_5 (melting point, 285 °C[37]) serves as a reactive flux that oxidizes the metal of interest and increases solubility to reduce reaction times and increase crystallite sizes. The vapor pressures of S and P would preclude reactions with significant excess because the pressures could rupture the fused-silica quartz ampules. When these elements are combined to prepare P_2S_5, the vapor pressure is reduced in the same temperature range, allowing this flux to be utilized at elevated temperatures. For all of the reactions attempted, no quartz ampule ruptured during the course of the heating profiles. As several systems were explored, the metal-to-P_2S_5 ratio was kept constant at 2:3. The remaining P_2S_5 flux was easily removed with a 1:1 mixture of ethanol and water, allowing for facile isolation of the product of interest. Eight different heating profiles were investigated with these systems and are referred to here as **Heating 1**, **2**, **3**, etc. (Table 2).

The bulk materials are generally air- and water-stable. The surfaces of the large single crystals remained lustrous after removal of the flux with an 50:50 (v/v) H_2O/EtOH solution. No degradation to the surface was visible after several weeks in air. $Mg_2P_2S_6$ dissolved in both DI water and the ethanol/water solution, but the solid is stable in dry air.

Variation of the Flux Synthesis with $Ni_2P_2S_6$ and $Co_2P_2S_6$ as Test Cases. The reactivity of the P_2S_5 flux was investigated by exploring different heating profiles for the Ni/P/S and Co/P/S systems, two systems with differing levels of synthetic difficulty. The rapidity of the flux reaction was apparent when using **Heating 8**, which resulted in phase-pure $Ni_2P_2S_6$ (Figure S7) with small crystallite sizes (<100 μm). Two reactions were used to elucidate the crystal growth of $Ni_2P_2S_6$, **Heating 3** and **4**, annealing at 650 °C and slow cooling from 650 °C. The largest crystals were formed from the day 4 annealing process, as seen in Figure 2a, reaching up

https://dx.doi.org/10.1021/acs.inorgchem.0c03577
Inorg. Chem. 2021, 60, 3502−3513

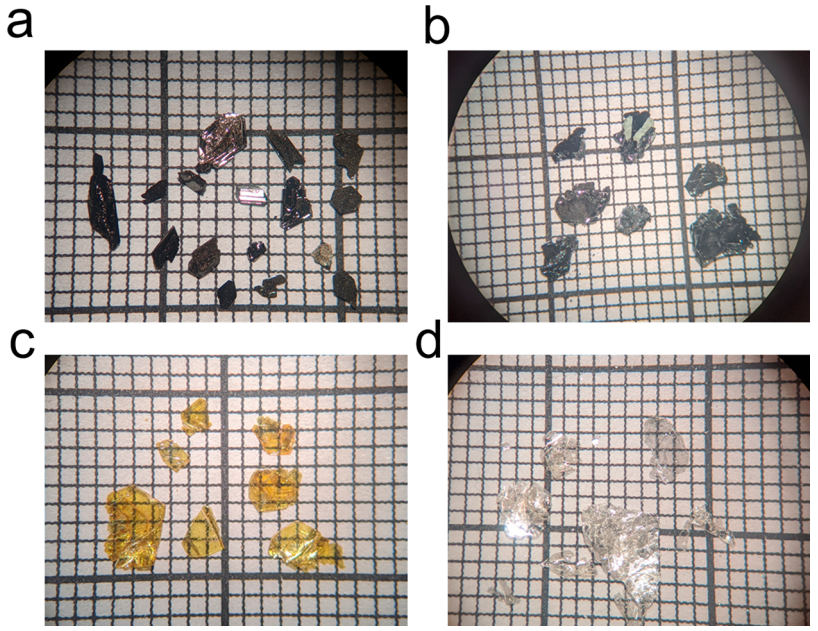

Figure 2. Optical images of (a) $Ni_2P_2S_6$, (b) $Co_2P_2S_6$, (c) $CuInP_2S_6$, (d) and $Zn_2P_2S_6$ single crystals. Each square is 1 × 1 mm^2.

to ~7 mm^2 in areal dimensions. The largest crystals from the day 4 cooling process were less than 1 mm^2 in all dimensions (Figure S2). However, a significant portion of the product was small crystallites, suggesting that some of the materials remained dissolved in the flux. **Heating 1**, which has both annealing and cooling stages, produced a phase-pure material (Figure 3a,b) with crystallites up to 1 mm in two dimensions. The reaction was scaled up by a factor of 10 to **Heating 1** and yielded a phase-pure material. All heating profiles produced phase-pure $Ni_2P_2S_6$; therefore, the ideal heating profile depends on the desired crystallite size and time constraints.

The synthesis of $Co_2P_2S_6$ is known to be more challenging than that of $Ni_2P_2S_6$ because part of the Co is sequestered in the $Co(P,S)_2$ phase. The literature reports that reaction times of up to 3 months are required to fully react with the $Co(P,S)_2$ phase. Four flux reactions (**Heating 1**, **2**, **5**, and **6**) were attempted to find the optimal synthesis method for $Co_2P_2S_6$. A two-phase mixture of $Co_2P_2S_6$ and $Co(P,S)_2$ formed under **Heating 1**, **5**, and **6**, although $Co(P,S)_2$ was only present in trace amounts (650, 540, and 580 °C) with **Heating 5**, forming the least amount of $Co(P,S)_2$, as seen in Figure S6. However, the size of the largest crystals varied as a function of the annealing temperature (580 °C), forming the largest crystals (Figure 2b). The annealing and cooling times for **Heating 2** were double those for **Heating 1** to enable longer reaction times. However, the main product of this reaction was $Co(P,S)_2$ with a trace of $Co_2P_2S_6$, which indicates the metastability of the $Co_2P_2S_6$ phase at 650 °C (Figure S6). The results from these different heating profiles indicate that **Heating 6** was the ideal heating profile for making large single crystals, while **Heating 5** made the most phase-pure material.

Flux Synthesis of Other Monometallic Thiophosphates. The synthesis of other $M_2P_2S_6$ layered phases was attempted using **Heating 1** and the same metal-to-P_2S_5 ratio. The polycrystalline products of these reactions were platelike crystals of various sizes (Figure S1). The Mn, Fe, Cd, and Mg reactions produced phase-pure compounds of green, black, clear, and clear color, respectively (Figures S4, S5, S9, and S10), while the Zn reaction produced $Zn_2P_2S_6$ and ZnS (Figure S8). However, large colorless crystals of $Zn_2P_2S_6$ (Figure 2d) could be mechanically separated. The 1-h reaction (**Heating 8**) produced small crystallites, and Mn and Fe reactions produced phase-pure materials (Figures S4 and S5). The 1-h Zn reaction produced $Zn_2P_2S_6$, $Zn_3(PS_4)_2$,[38] and ZnS (Figure S8). The small crystallite is reflected in the relatively low degree of preferred orientation, as indicated by the diffraction patterns.

Flux Synthesis of Bimetallic Thiophosphates. The $MM'P_2S_6$ solid solution bimetallic phases were targeted using a reaction with a metal-to-P_2S_5 ratio (M:M′:P_2S_5) of 1:1:3, using **Heating 1** and **5**. The six systems targeted were $MnFeP_2S_6$, $MnCoP_2S_6$, $MnNiP_2S_6$, $FeCoP_2S_6$, $FeNiP_2S_6$, and $CoNiP_2S_6$. The $MnCoP_2S_6$ and $FeCoP_2S_6$ phases have not been reported to the best of our knowledge. A representative powder pattern ($MnFeP_2S_6$, **Heating 1**) can be seen in Figure 3c,d. The PXRD patterns of the materials made at 650 and 540 °C (**Heating 1 and 5**, respectively) are shown in Figures S11−S16, respectively. These heating profiles produced phase-pure materials, although for the $MnNiP_2S_6$ system, the Bragg reflections were significantly broader than the other bimetallic phases for both heating profiles. This broadening suggests either a large strain or a distribution of layered phases with varying Mn/Ni ratios with slightly different lattice parameters.

The compositions of the $MM'P_2S_6$ products were probed using EDS analysis, and the results are shown in Figure 4. The (M + M′)-to-P-to-S ratio was consistently 1:1:3 through all of the bimetallic compounds. For the **Heating 5** (540 °C) reactions, two size distributions of crystals were apparent, and thus the chemical identities of both types of crystals were determined. Crystallites with dimensions of <50 μm typically had an M-to-M′ ratio close to 50:50, with Mn/Ni and Co/Ni deviating from the ideal ratio by 5% or more. The standard deviation (SD) was 5% or less for all combinations except Co/Ni with an SD of 8.5%. Substantial differences in the composition between large and small crystallites were observed for the Fe/Co (Fe 28[3]%; Co 72[3]%; SD > 100 μm) and Co/Ni (Co 70%; Ni 72.%; SD > 100 μm) systems. The results of the EDX measurements from all of the third-row transition-

https://dx.doi.org/10.1021/acs.inorgchem.0c03577
Inorg. Chem. 2021, 60, 3502−3513

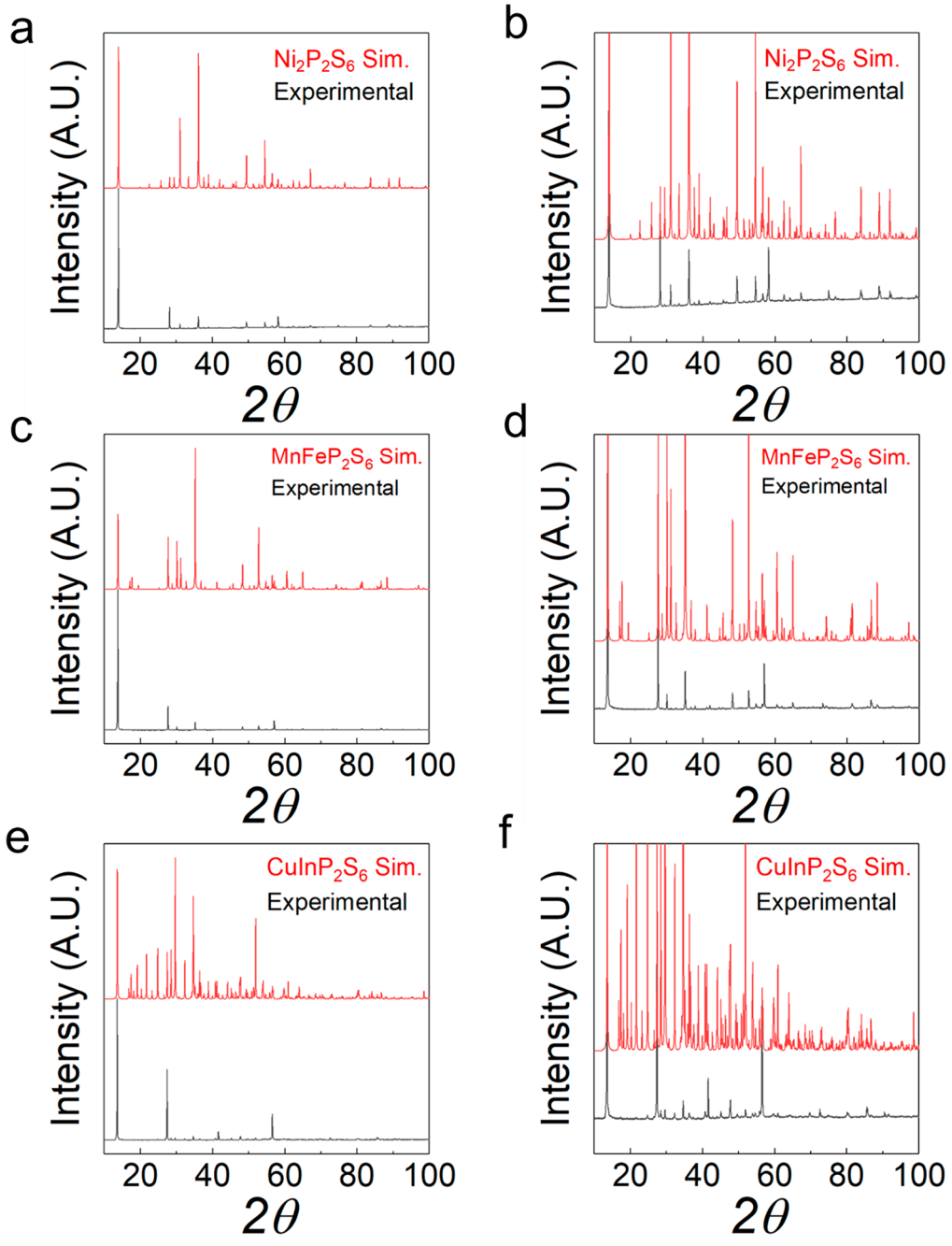

Figure 3. PXRD patterns of representative (a) monometallic ($Ni_2P_2S_6$, heating), (c) mixed occupied bimetallic ($MnFeP_2S_6$), and (e) ordered bimetallic ($CuInP_2S_6$) thiophosphates from **Heating 1**. The layered nature of these compounds results in significant preferred orientation, which causes a large discrepancy between the peak intensities of the experimental and simulated patterns. Even though the intensities do not match well, all peaks from the experimental patterns match with peaks from the simulated patterns seen in the zoomed in plots in parts b, d, and f.

metal bimetallic systems made using **Heating 1** (650 °C) collected on crystals with dimensions of less than 100 μm are shown in Figure 4. The M/M′ ratios for all systems made at 650 °C deviated by less than 5 atom % from the nominal 50 atom %.

Rietveld refinement of the PXRD data using GSAS II was used to determine the lattice parameters of the bimetallics shown in Table 3. Similar to the monometallic thiophosphates, the lattice parameters and unit cell volumes decreased as the average electron count increased, which follows the trend of decreasing ionic radius of the metal as the Z effectively increases. In theory, if the compositions are perfectly homogeneous with respect to the M/M′ ratio, the bimetallics made from two different heating profiles (650 vs 540 °C) would have the same unit cell volume. However, the unit cell volumes from the bimetallics made from **Heating 1** and **5** (650 and 540 °C) have differences in volumes of 1 Å^3 or less, except for the Mn/Ni and Co/Ni systems, with differences of 2.4 and 1.2 Å^3, respectively. These results suggest less homogeneity of bulk $MnNiP_2S_6$ and $CoNiP_2S_6$ depending on the heating profile used compared to the other bimetallic systems. The average unit cell volumes of the end members of the bimetallics listed in Table 3 and the experimental unit cell

https://dx.doi.org/10.1021/acs.inorgchem.0c03577
Inorg. Chem. 2021, 60, 3502−3513

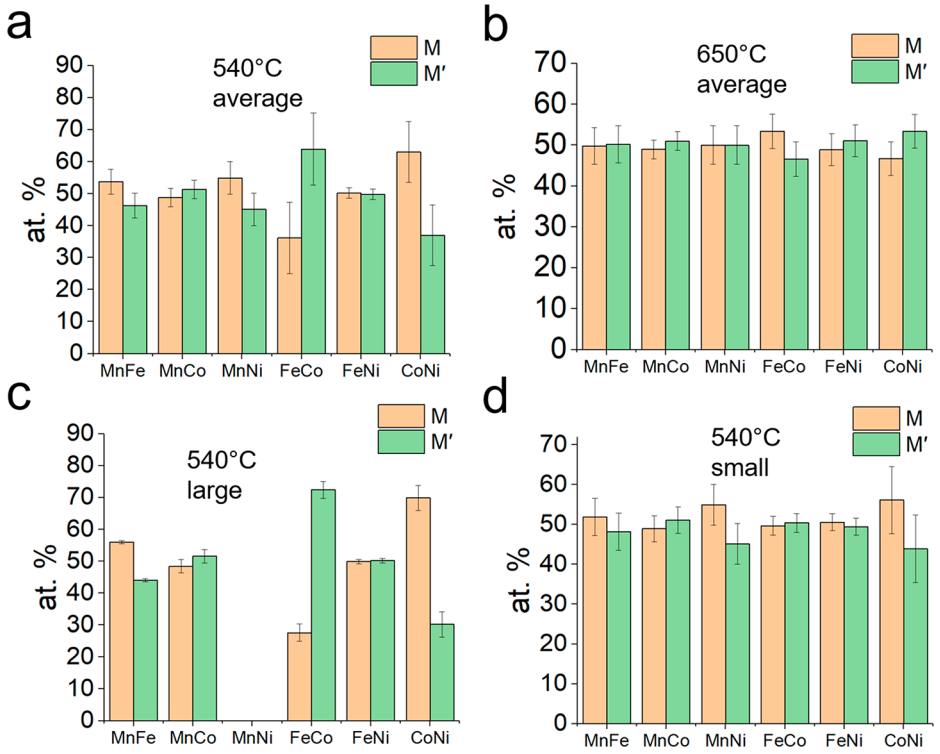

Figure 4. Average M and M′ atom % values of bimetallic thiophosphates synthesized using (a) **Heating 5** (540 °C) and (b) **Heating 1** (650 °C) derived from EDS spectra deconvoluted from P and S lines. M and M′ atom % values of bimetallic thiophosphates synthesized using **Heating 5** derived from EDS spectra deconvoluted from P and S lines from (c) "large" crystals (>100 μm in length) and (d) "small" crystals (typically <50 μm in length).

Table 3. Lattice Parameters and Unit Cell Volume of Mono- and Bimetallic Thiophosphates[a]

compound	a (Å)	b (Å)	c (Å)	β (deg)	volume (Å^3)	average volume between end members (Å^3)
$Mg_2P_2S_6$	6.071(19)	10.5134(8)	6.808(2)	107.175(6)	415.13(4)	N/A
$Mn_2P_2S_6$	6.083(3)	10.534(2)	6.801(2)	107.461(7)	415.74(9)	N/A
$Fe_2P_2S_6$	5.951(3)	10.302(2)	6.721(3)	107.214(9)	393.62(7)	N/A
$Co_2P_2S_6$	5.903(14)	10.2192(6)	6.668(16)	107.217(5)	384.21(2)	N/A
$Ni_2P_2S_6$	5.828(19)	10.087(10)	6.631(2)	107.104(6)	372.59(3)	N/A
$Zn_2P_2S_6$	5.978(9)	10.342(8)	6.751(9)	107.06(3)	399.1(2)	N/A
$Cd_2P_2S_6$	6.220(3)	10.768(17)	6.861(3)	107.395(9)	438.51(7)	N/A
$CuInP_2S_6$	6.098(2)	10.569(2)	13.627(7)	107.12(1)	839.2(2)	N/A
$MnFeP_2S_6$ (540 °C)	6.014(3)	10.425(16)	6.761(3)	107.165(8)	405.02(5)	404.68
$MnFeP_2S_6$ (650 °C)	6.010(17)	10.413(11)	6.756(17)	107.139(5)	404.06(4)	
$MnCoP_2S_6$ (540 °C)	5.991(2)	10.372(15)	6.738(2)	107.140(7)	400.13(4)	399.98
$MnCoP_2S_6$ (650 °C)	5.988(13)	10.3759(5)	6.736(15)	107.109(4)	399.98(3)	
$MnNiP_2S_6$ (540 °C)	5.979(3)	10.308(11)	6.741(3)	107.242(9)	396.76(5)	394.17
$MnNiP_2S_6$ (650 °C)	5.961(2)	10.2857(7)	6.732(2)	107.183(7)	394.32(3)	
$FeCoP_2S_6$ (540 °C)	5.922(16)	10.2597(8)	6.693(17)	107.108(5)	388.64(2)	388.92
$FeCoP_2S_6$ (650 °C)	5.921(14)	10.2581(6)	6.693(15)	107.099(4)	388.53(2)	
$FeNiP_2S_6$ (540 °C)	5.889(3)	10.202(2)	6.681(3)	107.075(9)	383.71(3)	383.11
$FeNiP_2S_6$ (650 °C)	5.881(14)	10.1969(5)	6.677(16)	107.028(5)	382.87(2)	
$CoNiP_2S_6$ (540 °C)	5.865(13)	10.1545(5)	6.651(15)	107.142(4)	378.49(18)	378.40
$CoNiP_2S_6$ (650 °C)	5.858(12)	10.1389(4)	6.647(14)	107.133(4)	377.25(2)	

[a]The average unit cell volumes of the end members of the bimetallic thiophosphates are shown in the last column for comparison.

volumes of the bimetallics were close in value, suggesting that the unit cell volumes adhere to Vegard's law.

The $CuInP_2S_6$ phase was synthesized by **Heating 1** and **7** with Cu, In, and P_2S_5, and using the elements at a ratio of 1:1:6:15 (Cu:In:P:S), respectively. The $CuInP_2S_6$ crystals grown from **Heating 7** are shown in Figure 2c, with the largest crystal having areal dimensions of 4 × 3 mm^2. The crystals from **Heating 1** produced crystals with dimensions slightly larger than 1 × 1 mm^2. The phase purity was confirmed via PXRD (Figure 3e,f).

In Situ PXRD Measurements. The reaction pathway for the formation of layered thiophosphate phases in the P_2S_5 flux was elucidated through in situ PXRD. The metal-to-P_2S_5 ratio for both reactions was the same as the ratios used for the bulk

https://dx.doi.org/10.1021/acs.inorgchem.0c03577
Inorg. Chem. 2021, 60, 3502−3513

syntheses. In these experiments, the reaction times were shortened, and the highest temperature was 550 °C because the fused-quartz capillary cannot withstand the pressures at 650 °C as well as those due to instrument limitations.

Ni/P_2S_5 System. The PXRD patterns collected during the Ni/P_2S_5 reaction are shown in Figure 5a. Ni metal and P_2S_5 are

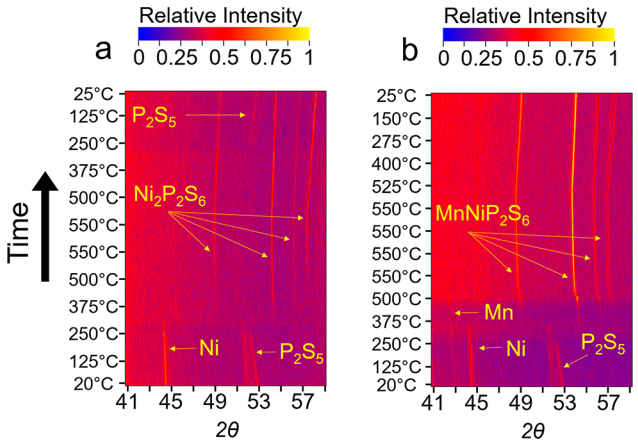

Figure 5. VT PXRD patterns of the (a) Ni/P_2S_5 and (b) Mn/Ni/P_2S_5 reactions.

both present at 20 °C. P_2S_5 melted first at 275 °C. Ni metal was consumed starting at approximately 325 °C, which initiated the formation of $Ni_2P_2S_6$ at approximately 375 °C. The reflections of $Ni_2P_2S_6$ became more intense as the reaction progressed to 550 °C. No other phases were observed during the annealing process. Upon cooling, P_2S_5 recrystallized at 250 °C. These results demonstrate the one-step formation of the compound with no competing undesirable nickel sulfide/phosphide phases. This highlights the effectiveness of the P_2S_5 flux in targeting the layered phases at a relatively low temperature. The direct formation of the layered $M_2P_2S_6$ phases from the reaction of the metal with the P_2S_5 flux is, therefore, a redox reaction in which P^{5+} oxidizes the metal to the M^{2+} state, forming the P^{4+} species of $[P_2S_6]^{4-}$ in situ, which then coordinates to the metal cation.

Mn/Ni/P_2S_5 System. The PXRD patterns collected during the Mn/Ni/P_2S_5 reaction are shown in Figure 5b. This bimetallic system was selected because the end-member-layered thiophosphate phases have a large difference in their lattice parameters; therefore, we wanted to examine whether there was preferential phase formation as a function of time. The phases present at 20 °C were Ni, Mn, and P_2S_5. At 275 °C, the P_2S_5 phase melted. The Ni metal was consumed at 350 °C, resulting in the formation of a layered thiophosphate phase. Up to 475 °C, the position of the most intense peak [(0 6 0)/(3 3 −1)] of the layered phase in this range was centered at the same 2θ angles as the corresponding peak of the layered phase of the pure Ni reaction, indicating that the layered phase formed first was Ni-rich (Figure S35a). The main peak from Mn (2θ = 43° at 20 °C) was close to the background but was consumed at approximately 525 °C. From 475 to 550 °C, the (0 6 0)/(3 3 −1) reflection of the layered thiophosphate phase decreased to a relatively low 2θ, not only from thermal expansion but also from the incorporation of the relatively large Mn into the layered phase (Figure S35b). During the annealing stage, the (0 6 0)/(3 3 −1) reflection of the layered phase continued to shift to a relatively low 2θ, as seen in Figure S35c, suggesting that Mn was incorporated into the thiophosphate structure. In contrast to the Ni reaction, P_2S_5 did not recrystallize upon cooling.

Optical Properties. The resulting $M_2P_2S_6$ products from our synthesis described above were characterized by optical absorption spectroscopy. The complex electronic structure of 3d metal-layered thiophosphates manifested with equally complex optical properties. The weakly interacting model developed by the early work from Khumalo and Hughes[39] and Piacentini et al.[40] argues that the 3d M^{2+} cations are nonbonding; thus, the d orbitals located in and around the energy gap of the P,S 3p manifold (see ref 41 for the positions of these orbitals) can produce optical transitions with energies determined by the crystal-field splitting of the free ion. In addition, transitions can occur from the P,S $3p_{x,y}$ orbitals to the empty 3d orbitals of the metal cations (charge transfer) or from the empty 3d orbitals to the antibonding bands (orbital promotion). The origin of these transitions is further complicated because partial hybridization of the ligand orbitals with 3d orbitals close to energy can occur, as seen in $Fe_2P_2S_6$.[42] Thus, optical absorption of the true band gap may be convoluted with these various optical transitions. When the bimetallic system is considered, more complexities ensue. Therefore, we tabulated the highest-energy absorption edges but remained noncommittal to ascribing it to the optical band gap.

The optical absorption is shown in Figure 6a−c for all thiophosphate compounds synthesized in this study. The highest-energy absorption edges are listed in Table 4 and compared to previously reported values. A common feature of the optical absorption spectra of the thiophosphates containing unfilled d-orbital shells is a peak feature typically centered at 1 eV (2 eV for $Mn_2P_2S_6$), which is well separated with a transition from the putative valence to the conduction band (with the unpaired d electrons not being there). These peaks arose from the electronic transitions involving the d orbitals described above. $FeCoP_2S_6$ did not feature a peak, although the onset of the absorption edge was similar to that of the other thiophosphate compounds. A better understanding of the optical transitions of these compounds, especially the bimetallics, will require careful theoretical calculations and experimental studies, such as X-ray photoelectron spectroscopy studies, which are currently beyond the scope of this paper.

The absorption spectra of the $CuInP_2S_6$, $Zn_2P_2S_6$, and $Cd_2P_2S_6$ samples are shown in Figure 6c. These compounds have filled d-orbital shells that preclude d → d and charge-transfer transitions. The energy scheme[43] developed for $Cd_2P_2S_6$ places the 4d states deep in the valence band, meaning that optical absorptions involving orbital promotion would be in the deep-UV region. Thus, the fundamental absorption of $Cd_2P_2S_6$ in this energy range was attributed to the interband transition from the top of the valence band to the bottom of the conduction band.

The work function of all of the layered thiophosphates was determined using PYSA, as shown in Figures S36 and S37. The work function values (Table 4) represent the energy levels of the top of the valence bands, given the wide-gap semiconducting character of the compounds. They all fall within the range of 5.24−5.72 eV, which is reasonable given that the orbital character of the valence band is mainly the filled p state of the S orbitals. Knowledge of the work function will be useful in choosing metal contacts for device fabrication.

https://dx.doi.org/10.1021/acs.inorgchem.0c03577
Inorg. Chem. 2021, 60, 3502−3513

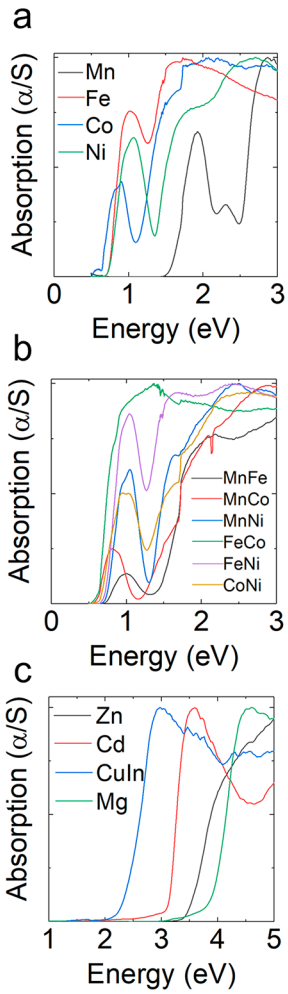

Figure 6. Optical absorption spectra of unfilled 3d transition-metal (a) monometallic ($M_2P_2S_6$), where the label in the graph corresponds to M, and (b) bimetallic ($MM'P_2S_6$), where the label in the graph corresponds to MM′, and (c) filled d^{10} metal thiophosphates, where the label in the graph corresponds to M in $M_2P_2S_6$ and $CuInP_2S_6$.

Table 4. Optical Band Gap and Work Function for Mono- and Bimetallic Thiophosphates at Room Temperature

compound	highest-energy absorption edge (eV)	reported highest-energy absorption edge (eV)	work function (eV)
$Mg_2P_2S_6$	3.90	N/A	N/A
$Mn_2P_2S_6$	2.47	3.0[46]	5.39
$Fe_2P_2S_6$	0.99	1.6,[46] 1.5[47]	5.28
$Co_2P_2S_6$	1.09	N/A	5.72
$Ni_2P_2S_6$	1.29	1.7[47]	5.44
$Zn_2P_2S_6$	3.50	3.4[46]	5.54
$Cd_2P_2S_6$	3.13	3.0[43]	5.50
$MnFeP_2S_6$	1.42	N/A	5.40
$MnCoP_2S_6$	1.18	N/A	5.37
$MnNiP_2S_6$	1.29	N/A	5.26
$FeCoP_2S_6$	0.62	N/A	5.24
$FeNiP_2S_6$	1.08	N/A	5.31
$CoNiP_2S_6$	1.08	N/A	5.57
$CuInP_2S_6$	2.39	2.7[48]	5.35

TEM Studies of $Ni_2P_2S_6$, $Mn_2P_2S_6$, and $MnNiP_2S_6$ as Test Cases. TEM images and SAED patterns taken perpendicular to the *ab* plane/along the *c** axis of $Ni_2P_2S_6$, $Mn_2P_2S_6$, and $MnNiP_2S_6$ show nearly perfect sets of rotational symmetry patterns of a hexagonal crystal, indicating that each flake is a highly single crystal (Figure 7a–c). The *c** axis is approximately parallel to the [103]-zone axis, and the simulated SAED patterns of $Ni_2P_2S_6$ along the [103]-zone axis are shown in Figure S38b–d and are rotated 120° and 240° about the [103]-zone axis, respectively. Merging the three SAED patterns into Figure S38a results in a diffraction pattern with 120° rotational twins. This pattern agrees most with the experimental SAED patterns and accounts for the pseudohexagonal symmetry observed in the SAED patterns of $Ni_2P_2S_6$, $Mn_2P_2S_6$, and $MnNiP_2S_6$. Murayama et al. conducted a study on $Fe_2P_2S_6$ and also observed 120° rotational twins that account for a "pseudo-hexagonal" symmetry along the *c**-zone axis.[44] TEM images of $Ni_2P_2S_6$, $Mn_2P_2S_6$, and $MnNiP_2S_6$ reveal the layered character of these three systems as well as the strain contrast due to the exfoliation process (Figure S39a–c). Representative HRTEM images taken from the thin regions near the edge of each respective flake from Figure S39a–c are shown in Figure 7d–f, with the 1/3(39$\bar{1}$)-lattice planes indicated.

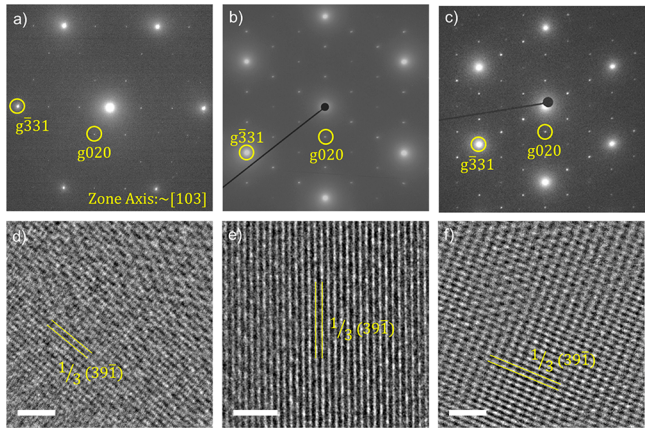

Figure 7. (a–c) SAED patterns for $Ni_2P_2S_6$, $Mn_2P_2S_6$, and $MnNiP_2S_6$, respectively, along the *c** axis, which is nearly parallel with the [103] axis and is indicated as such. (d–f) HRTEM images of $Ni_2P_2S_6$, $Mn_2P_2S_6$, and $MnNiP_2S_6$ along the *c** axis, with 1/3(39$\bar{1}$) planes indicated. The scale bars are all 2 nm in length.

The average stoichiometry and chemical uniformity at the nanometer range of $Ni_2P_2S_6$, $Mn_2P_2S_6$, and $MnNiP_2S_6$ flakes were evaluated using STEM–EDS maps (Figure S40). The measured nominally proportional stoichiometry of $Ni_2P_2S_6$ and $Mn_2P_2S_6$ reasonably matches the expected values of 1:1:3 for (Ni/Mn)/P/S, respectively, as shown in the top and middle rows of Figure S40. However, for a mixed Mn/Ni alloyed system, $MnNiP_2S_6$, the measured nominally proportional atomic percentages deviated from the expected ratio of 1:1:2:6 for Mn/Ni/P/S with atomic percentages at 5.9 atom % Ni, 13.5 atom % Mn, 20.0 atom % P, and 60.6 atom % S. Because the P and S atom % values are consistent with the expected values and the SAED pattern of the $MnNiP_2S_6$ flake shows high single crystallinity, the elemental analyses may indicate possible inhomogeneity within the sample. More detailed study is required to understand the possible solid solubility range within these bimetallic systems. The colored maps denoting Ni in yellow, Mn in orange, P in red, and S in green show a homogeneous EDS signal throughout each flake at the given resolution.

https://dx.doi.org/10.1021/acs.inorgchem.0c03577
Inorg. Chem. 2021, 60, 3502–3513

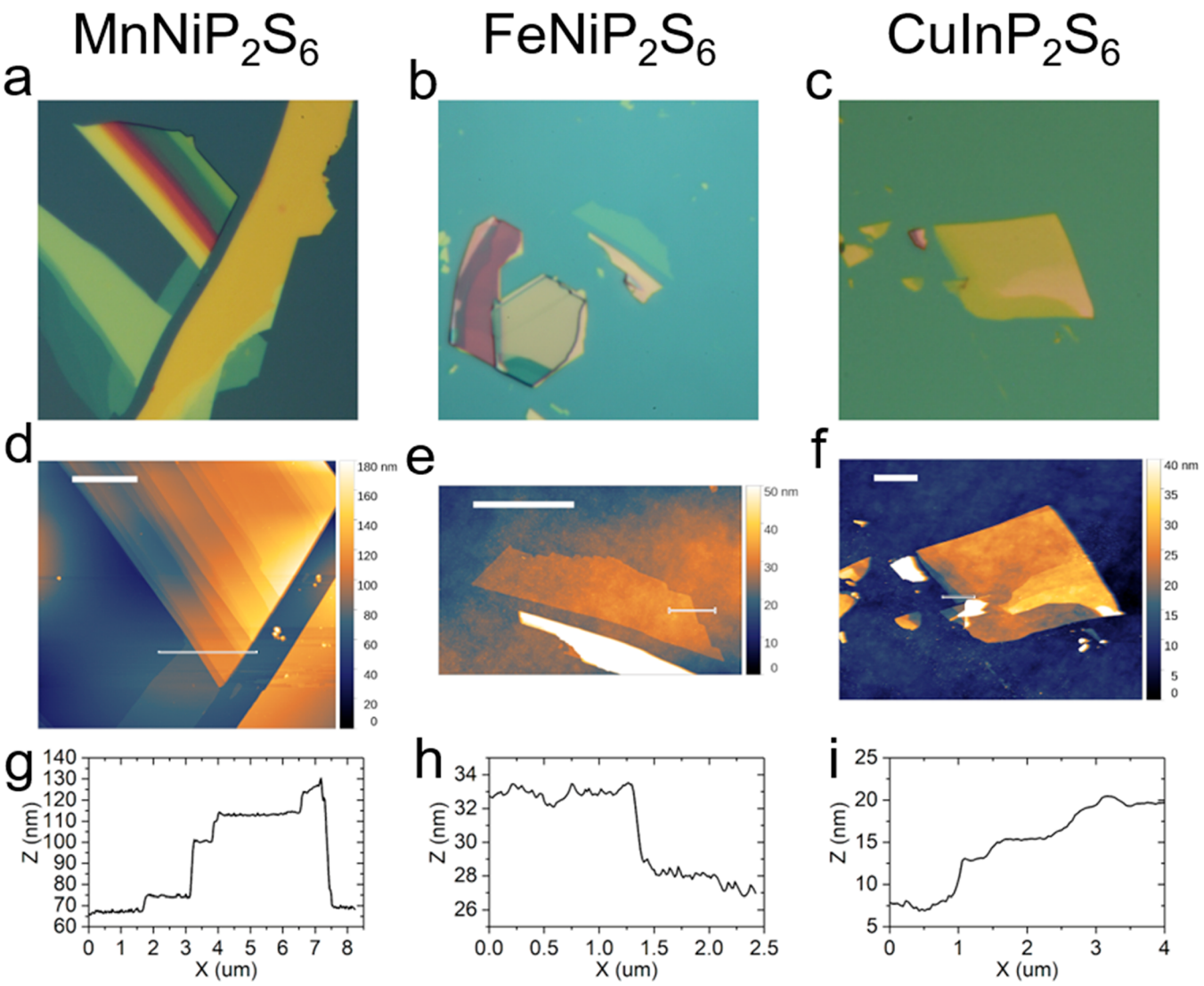

Figure 8. Representative (a–c) optical and (d–f) AFM images of thiophosphate flakes. The scale bars are 5 μm in length. Plots of the height profile (g–i) along the lines highlighted in the AFM scans.

Exfoliation and Transport Measurements on Bimetallic Thiophosphates. As layered/vdW materials, the thiophosphates are known to be readily cleaved down to individual layers when mechanically exfoliated. The now-famous "scotch-tape method" benefits from the use of large-area crystals that experience a more uniform adhesive force, resulting in substantially larger and more pristine few-layer flakes on the final substrate. To assess the viability of the crystals grown in this work for the fabrication of thin-film samples and vdW heterostructures, we performed a series of such exfoliations using commercially available poly(vinyl chloride) (PVC) tape or PDMS film. Following cleavage, the flakes adhered to 330 nm SiO_x-coated p-type Si wafers for optical identification by bright-field/dark-field-reflected light microscopy. As a preliminary metric, the thickness can be roughly assessed by the layer-dependent coloration present in most vdW materials below 250 nm thickness, with thinner flakes becoming increasingly transparent in appearance. As seen in Figure 8a,b,c, crystalline flakes demonstrate good color contrast against the 330 nm oxide substrate and require little process optimization to produce large-area thin films. Subsequently, the adhesive residue was removed by gently washing the substrates with acetone, methanol, and isopropyl alcohol, and the thickness can be assessed via NC-AFM. In Figure 8d,e,f, we verify the yields of <20 nm thin films in preliminary exfoliations.

The ease of exfoliation and prevalence of exfoliated flakes below 20 nm thickness indicates good physical stability for the purposes of vdW film characterization and functionalization in 2D devices. Large crystals can be readily cleaved into thin films (<100um) using tape, which hold their shape well even under modest bending/twisting. In this manner, up to 1-cm-long sheets of ~10 μm thickness can be obtained by hand under a stereomicroscope. Most exfoliated samples do not change in appearance or disintegrate in air or during lithographic processing (in the presence of organic solvents, water, polymers, etc.). The lack of visible degradation indicates at least moderate air stability relative to other vdW materials.

To produce larger samples for room temperature IV studies, we similarly cleaved as-grown crystals in 2 mm × 2 mm × 5–25 μm sheets using PVC tape. Because these crystals appear to be remarkably flexible when thinned down, they can be easily handled. Using a two-terminal electrode configuration, the observed estimates of the resistance across all samples indicate

https://dx.doi.org/10.1021/acs.inorgchem.0c03577
Inorg. Chem. 2021, 60, 3502–3513

extremely high resistance (over 200 GΩ) under gate biases of up to ±60 V. No significant ferroelectric-type switching was observed over swept voltages of up to ±10 V, indicating the absence of local ionic motions. Subsequently, the films were exposed to DEMI-TFSI-based ionic liquid gel (ILG), which when used as a gate provides substantial doping over a ±3 V range (at relatively high voltages, it begins to decompose). Despite gating, little change in the two-terminal resistance or swept IV behavior was seen in the measured samples. The minimum resistance measured on a 30-nm-thick $MnNiP_2S_6$ sample from a two-terminal resistive measurement across 70 μm separated Pd/Au leads with a ILG gating of 3 V was 2 GΩ. We believe these results are concordant with the Mott-insulating behavior expected of very clean thiophosphates.

CONCLUSIONS

The P_2S_5 flux provides reactive media for the direct formation of layered thiophosphate phases, enabling quicker reaction times compared to stoichiometric reactions. In general, shorter reaction times will result in smaller crystallites because there is less time for crystallites to grow. The sizes of the crystals ranged from a few microns to dimensions of several square millimeters, which can be mechanically separated. This variety of sizes will prove useful for applications that require a specific size distribution, e.g., catalysis and intercalation studies. The annealing temperature is also an important parameter to consider because certain thiophosphates may decompose at elevated temperatures. The synthetic conditions presented here are by no means exhaustive. Rather, we see this study as a starting point for the reader to further explore this reaction space based on the need of the reader. The reactions explored here do at least provide a more efficient route to making phase-pure materials for most of the systems studied here. We recommend for new systems starting off with **Heating 1** and then fine-tuning the reaction depending on the obtained products. In addition, two novel bimetallics, $MnCoP_2S_6$ and $FeCoP_2S_6$, were discovered. TEM and AFM studies demonstrated that high-quality materials can be synthesized using this flux technique. Although we have only demonstrated a few select systems, we anticipate that this general method will facilitate the expansion of other metal thiophosphate materials, such as main-group-metal monometallics, main-group/transition-metal bimetallics, and 3d/4d transition-metal bimetallics.

ASSOCIATED CONTENT

Supporting Information

The Supporting Information is available free of charge at https://pubs.acs.org/doi/10.1021/acs.inorgchem.0c03577.

Supplemental experimental information, pictures of bulk material and crystals from various syntheses, PXRD patterns from all material produced, SEM images and EDS values from bimetallic syntheses, full range of VT PXRD patterns for Ni/P_2S_5 and $Mn/Ni/P_2S_5$ reactions, photoemission yield spectra in air for each metal thiophosphate, simulated SAED patterns, bright-field TEM images, and annular dark-field STEM images (PDF)

AUTHOR INFORMATION

Corresponding Author

Mercouri G. Kanatzidis − *Department of Chemistry, Northwestern University, Evanston, Illinois 60208, United States;* orcid.org/0000-0003-2037-4168; Email: m-kanatzidis@northwestern.edu

Authors

Daniel G. Chica − *Department of Chemistry, Northwestern University, Evanston, Illinois 60208, United States;* orcid.org/0000-0001-8616-9365

Abishek K. Iyer − *Department of Chemistry, Northwestern University, Evanston, Illinois 60208, United States;* orcid.org/0000-0002-8582-3895

Matthew Cheng − *Department of Material Science and Engineering, Northwestern University, Evanston, Illinois 60208, United States*

Kevin M. Ryan − *Department of Physics and Astronomy, Northwestern University, Evanston, Illinois 60208, United States*

Patrick Krantz − *Department of Physics and Astronomy, Northwestern University, Evanston, Illinois 60208, United States*

Craig Laing − *Department of Chemistry, Northwestern University, Evanston, Illinois 60208, United States;* orcid.org/0000-0002-0654-4741

Roberto dos Reis − *Department of Material Science and Engineering and Northwestern University Atomic and Nanoscale Characterization Experimental (NUANCE) Center, Northwestern University, Evanston, Illinois 60208, United States*

Venkat Chandrasekhar − *Department of Physics and Astronomy, Northwestern University, Evanston, Illinois 60208, United States*

Vinayak P. Dravid − *Department of Material Science and Engineering, Northwestern University Atomic and Nanoscale Characterization Experimental (NUANCE) Center, and International Institute for Nanotechnology (IIN), Northwestern University, Evanston, Illinois 60208, United States;* orcid.org/0000-0002-6007-3063

Complete contact information is available at: https://pubs.acs.org/10.1021/acs.inorgchem.0c03577

Notes

The authors declare no competing financial interest.

ACKNOWLEDGMENTS

This work was supported, in part, by the Army Research Office (Grant W911NF1910335). This work made use of the EPIC facility of Northwestern University's NUANCE Center, which has received support from the SHyNE Resource [National Science Foundation (NSF) Grant ECCS-2025633], Northwestern's MRSEC program (NSF Grant DMR-1720139), the Keck Foundation, and the State of Illinois through IIN. This material is based on work supported by the NSF Graduate Research Fellowship under Grant DGE-1842165 and the NSF Division of Material Research (NSF Grant DMR-1929356)

REFERENCES

(1) Susner, M. A.; Chyasnavichyus, M.; Mcguire, M. A.; Ganesh, P.; Maksymovych, P. Metal Thio- and Selenophosphates as Multifunctional van Der Waals Layered Materials. *Adv. Mater.* **2017**, *29*, 1602852.

(2) Wang, F.; Shifa, T. A.; Yu, P.; He, P.; Liu, Y.; Wang, F.; Wang, Z.; Zhan, X.; Lou, X.; Xia, F.; He, J. New Frontiers on van Der Waals Layered Metal Phosphorous Trichalcogenides. *Adv. Funct. Mater.* **2018**, *28* (37), 1802151.

(3) Ouvrard, G.; Brec, R.; Rouxel, J. Structural Determination of Some MPS3 Layered Phases (M = Mn, Fe, Co, Ni and Cd). *Mater. Res. Bull.* **1985**, *20* (10), 1181−1189.
(4) Wildes, A. R.; Simonet, V.; Ressouche, E.; McIntyre, G. J.; Avdeev, M.; Suard, E.; Kimber, S. A. J.; Lançon, D.; Pepe, G.; Moubaraki, B.; Hicks, T. J. Magnetic Structure of the Quasi-Two-Dimensional Antiferromagnet NiPS3. *Phys. Rev. B: Condens. Matter Mater. Phys.* **2015**, *92* (22), 1−11.
(5) Lee, J. U.; Lee, S.; Ryoo, J. H.; Kang, S.; Kim, T. Y.; Kim, P.; Park, C. H.; Park, J. G.; Cheong, H. Ising-Type Magnetic Ordering in Atomically Thin FePS3. *Nano Lett.* **2016**, *16* (12), 7433−7438.
(6) Onga, M.; Sugita, Y.; Ideue, T.; Nakagawa, Y.; Suzuki, R.; Motome, Y.; Iwasa, Y. Antiferromagnet − Semiconductor Van Der Waals Heterostructures: Interlayer Interplay of Exciton with Magnetic Ordering. *Nano Lett.* **2020**, *20* (6), 4625−4630.
(7) Liu, F.; You, L.; Seyler, K. L.; Li, X.; Yu, P.; Lin, J.; Wang, X.; Zhou, J.; Wang, H.; He, H.; Pantelides, S. T.; Zhou, W.; Sharma, P.; Xu, X.; Ajayan, P. M.; Wang, J.; Liu, Z. Room-Temperature Ferroelectricity in CuInP 2 S 6 Ultrathin Flakes. *Nat. Commun.* **2016**, *7*, 1−6.
(8) Harms, N. C.; Kim, H. S.; Clune, A. J.; Smith, K. A.; O'Neal, K. R.; Haglund, A. V.; Mandrus, D. G.; Liu, Z.; Haule, K.; Vanderbilt, D.; Musfeldt, J. L. Piezochromism in the Magnetic Chalcogenide MnPS3. *npj Quantum Mater.* **2020**, *5* (1), 1−7.
(9) Wang, Y.; Zhou, Z.; Wen, T.; Zhou, Y.; Li, N.; Han, F.; et al. Pressure-Driven Cooperative Spin-Crossover, Large-Volume Collapse, and Semiconductor-to-Metal Transition in Manganese(II) Honeycomb Lattices. *J. Am. Chem. Soc.* **2016**, *138* (48), 15751−15757.
(10) Kim, H.; Haule, K.; Vanderbilt, D. Mott Metal-Insulator Transitions in Pressurized Layered Trichalcogenides. *Phys. Rev. Lett.* **2019**, *123* (23), 236401.
(11) Ismail, N.; El-meligi, A. A.; Temerk, Y. M.; Madian, M. Synthesis and Characterization of Layered FePS 3 for Hydrogen Uptake. *Int. J. Hydrogen Energy* **2010**, *35* (15), 7827−7834.
(12) Song, B.; Li, K.; Yin, Y.; Wu, T.; Dang, L.; Cában-Acevedo, M.; Han, J.; Gao, T.; Wang, X.; Zhang, Z.; Schmidt, J. R.; Xu, P.; Jin, S. Tuning Mixed Nickel Iron Phosphosulfide Nanosheet Electrocatalysts for Enhanced Hydrogen and Oxygen Evolution. *ACS Catal.* **2017**, *7*, 8549−8557.
(13) Chang, J.; Wang, G.; Belharsa, A.; Ge, J.; Xing, W.; Yang, Y. Stable $Fe_2P_2S_6$ Nanocrystal Catalyst for High-Efficiency Water Electrolysis. *Small Methods* **2020**, *4*, 1900632.
(14) Lv, R.; Robinson, J. A.; Schaak, R. E.; Sun, D.; Sun, Y.; Mallouk, T. E.; Terrones, M. Transition Metal Dichalcogenides and beyond: Synthesis, Properties, and Applications of Single- and Few-Layer Nanosheets. *Acc. Chem. Res.* **2015**, *48* (1), 56−64.
(15) Novoselov, K. S.; Geim, A. K.; Morozov, S. V.; Jiang, D.; Zhang, Y.; Dubonos, S. V.; G, I. V.; F, A. A. *Science* **2004**, *306* (5696), 666−669.
(16) Chica, D. G.; He, Y.; Mccall, K. M.; Chung, D. Y.; Pak, R. O.; Trimarchi, G.; Liu, Z.; De Lurgio, P. M.; Wessels, B. W.; Kanatzidis, M. G. Direct Thermal Neutron Detection by the 2D Semiconductor 6LiInP2Se6. *Nature* **2020**, *577*, 346−349.
(17) Gave, M. A.; Bilc, D.; Mahanti, S. D.; Breshears, J. D.; Kanatzidis, M. G. On the Lamellar Compounds CuBiP2Se6, AgBiP 2Se6 and AgBiP2S6. Antiferroelectric Phase Transitions Due to Cooperative Cu+ and Bi3+ Ion Motion. *Inorg. Chem.* **2005**, *44* (15), 5293−5303.
(18) Pfeiff, R.; Kniep, R. Quaternary Selenodiphosphates(IV): MIMIII[P2Se6], (MI = Cu, Ag; MIII = Cr, Al, Ga, In). *J. Alloys Compd.* **1992**, *186*, 111−133.
(19) Galdamez, A.; Manriquez, V.; Kasaneva, J.; Avila, R. E. Synthesis, Characterization and Electrical Properties of Quaternary Selenodiphosphates : AMP2Se6 with A = Cu, Ag and M = Bi, Sb. *Mater. Res. Bull.* **2003**, *38*, 1063−1072.
(20) Kuhn, A.; Eger, R.; Nuss, J.; Lotsch, B. V. Synthesis and Crystal Structures of the Alkali Aluminium Thiohypodiphosphates MIAlP2S6 (M = Li, Na). *Z. Anorg. Allg. Chem.* **2013**, *639*, 1087−1089.
(21) Ouili, Z.; Leblanc, A.; Colombet, P. Crystal Structure of a New Lamellar Compound : Ag1/2In1/2PS3. *J. Solid State Chem.* **1987**, *66*, 86−94.
(22) Maisonneuve, V.; Cajipe, V. B.; Payen, C. Low-Temperature Neutron Powder Diffraction Study of CuCrP2S6 : Observation of an Ordered, Antipolar Copper Sublattice. *Chem. Mater.* **1993**, *5*, 758−760.
(23) Goossens, D. J.; Hicks, T. J. The Magnetic Phase Diagram of MnxZn1-XPS3. *J. Phys.: Condens. Matter* **1998**, *10*, 7643−7652.
(24) Bhutani, A.; Zuo, J. L.; McAuliffe, R. D.; Dela Cruz, C. R.; Shoemaker, D. P. Strong Anisotropy in the Mixed Antiferromagnetic System Mn1-XFexPSe3. *Phys. Rev. Mater.* **2020**, *4* (3), 34411.
(25) Kliche, G. *Z. Naturforsch., A: Phys. Sci.* **1983**, *38*, 1133−1137.
(26) Manríquez, V.; Barahona, P.; Peña, O. Physical Properties of the Cation-Mixed M′MPS3 Phases. *Mater. Res. Bull.* **2000**, *35* (11), 1889−1895.
(27) Rao, R. R.; Raychaudhuri, A. K. Magnetic Studies of a Mixed Antiferromagnetic System Fe1-XNixPS3. *J. Phys. Chem. Solids* **1992**, *53* (4), 577−583.
(28) He, Y.; Dai, Y.; Huang, H.; Lin, J.; Hsia, Y. *J. Alloys Compd.* **2003**, *359*, 41−45.
(29) Yan, X.; Chen, X.; Qin, J. Synthesis and Magnetic Properties of New Layered $Ni_xMn_{1-x}PS_3$ and Their Intercalation Compounds. *Acta Chim. Sin.* **2011**, *69* (8), 1017−1023.
(30) Brec, R. Review on Structural and Chemical Properties of Transition Metal Phosphorous Trisulfides MPS3. *Solid State Ionics* **1986**, *22*, 3−30.
(31) Mayorga-Martinez, C. C.; Sofer, Z.; Sedmidubsky, D.; Huber, S.; Eng, A. Y. S.; Pumera, M. Layered Metal Thiophosphite Materials: Magnetic, Electrochemical, and Electronic Properties. *ACS Appl. Mater. Interfaces* **2017**, *9*, 12563−12573.
(32) Dangol, R.; Dai, Z.; Chaturvedi, A.; Zheng, Y.; Zhang, Y.; Dinh, K. N.; Li, B.; Zong, Y.; Yan, Q. Few-Layer NiPS3 Nanosheets as Bifunctional Materials for Li-Ion Storage and Oxygen Evolution Reaction. *Nanoscale* **2018**, *10*, 4890−4896.
(33) Wildes, A. R.; Simonet, V.; Ressouche, E.; Ballou, R.; McIntyre, G. J. The Magnetic Properties and Structure of the Quasi-Two-Dimensional Antiferromagnet CoPS3. *J. Phys.: Condens. Matter* **2017**, *29*, 455801.
(34) Kanatzidis, M. G. Discovery-Synthesis, Design, and Prediction of Chalcogenide Phases. *Inorg. Chem.* **2017**, *56* (6), 3158−3173.
(35) Kanatzidis, M. New Directions in Synthetic Solid State Chemistry: Chalcophosphate Salt Fluxes for Discovery of New Multinary Solids. *Curr. Opin. Solid State Mater. Sci.* **1997**, *2* (2), 139−149.
(36) Aitken, J. A.; Brown, S.; Chondroudis, K.; Jobic, S.; Brec, R.; Kanatzidis, M. G. β-Bi4(P2Se6)3: A New Ternary Selenophosphate Obtained in a P2Se5 Flux. *Inorg. Chem.* **1999**, *38* (21), 4795−4800.
(37) Okamoto, H. P-S (Phosphorus-Sulfur). *J. Phase Equilib.* **1991**, *12* (6), 706−707.
(38) Jörgens, S.; Johrendt, D.; Mewis, A. Motive Dichtester Kugelpackungen: Die Verbindungen Zn 3(PS 4) 2 Und LiZnPS 4. *Z. Anorg. Allg. Chem.* **2002**, *628* (8), 1765−1769.
(39) Khumalo, F. S.; Hughes, H. P. Reflectance Spectra of Some FePS3-Type Layer Compounds in the Vacuum Ultraviolet. *Phys. Rev. B: Condens. Matter Mater. Phys.* **1981**, *23* (10), 5375−5383.
(40) Grasso, V.; Santangelo, S.; Piacentini, M. Optical Absorption Spectra of Some Transition Metal Thiophosphates. *Solid State Ionics* **1986**, *20* (1), 9−15.
(41) Kurita, N.; Nakao, K. Band Structures and Physical Properties of Magnetic Layered Semiconductors MPS3. *J. Phys. Soc. Jpn.* **1989**, *58* (2), 610−621.
(42) Choi, W. K.; Kneedler, E.; Kevan, S. D. Delocalization of the Fe 3d Levels in the Quasi-Two-Dimensional Correlated Insulator FePS3. *Phys. Rev. B: Condens. Matter Mater. Phys.* **1994**, *50* (20), 15276−15286.
(43) Calareso, C.; Grasso, V.; Silipigni, L. Optical Spectra of the Layered Cd P S and Cd P Se Compounds in the Region from 1. 6 to 5. 5 EV. *J. Appl. Phys.* **1997**, *82* (12), 6228−6234.

https://dx.doi.org/10.1021/acs.inorgchem.0c03577
Inorg. Chem. 2021, 60, 3502−3513

(44) Murayama, C.; Okabe, M.; Urushihara, D.; Asaka, T.; Fukuda, K.; Isobe, M.; Yamamoto, K.; Matsushita, Y. Crystallographic Features Related to a van Der Waals Coupling in the Layered Chalcogenide FePS3. *J. Appl. Phys.* **2016**, *120* (14), 142114.
(45) Jörgens, S.; Mewis, A. Die Kristallstrukturen von Hexachalcogeno-Hypodiphosphaten Des Magnesiums Und Zinks. *Z. Anorg. Allg. Chem.* **2004**, *630* (1), 51−57.
(46) Brec, R.; Schleich, D. M.; Ouvrard, G.; Louisy, A.; Rouxel, J. Physical Properties of Lithium Intercalation Compounds of the Layered Transition Chalcogenophosphates. *Inorg. Chem.* **1979**, *18* (7), 1814−1818.
(47) Foot, P. J. S.; Suradi, J.; Lee, P. A. Optical and Electronic Properties of the Layered Semiconductors NiPS3 and FePS3. *Mater. Res. Bull.* **1980**, *15* (2), 189−193.
(48) Studenyak, I. P.; Mitrovcij, V. V.; Kovacs, G. S.; Gurzan, M. I.; Mykajlo, O. A.; Vysochanskii, Yu. M.; Cajipe, V. B. Disordering effect on optical absorption processes in CuInP2S6 layered ferrielectrics. *Phys. Status Solidi B* **2003**, *236* (3), 678−686.
(49) Maisonneuve, V.; Evain, M.; Payen, C.; Cajipe, V. B.; Molinié, P. Room-Temperature Crystal Structure of the Layered Phase CuIInIIIP2S6. *J. Alloys Compd.* **1995**, *218* (2), 157−164.

https://dx.doi.org/10.1021/acs.inorgchem.0c03577
Inorg. Chem. 2021, 60, 3502−3513